

Manuscript version: Author's Accepted Manuscript

The version presented in WRAP is the author's accepted manuscript and may differ from the published version or Version of Record.

Persistent WRAP URL:

<http://wrap.warwick.ac.uk/153863>

How to cite:

Please refer to published version for the most recent bibliographic citation information. If a published version is known of, the repository item page linked to above, will contain details on accessing it.

Copyright and reuse:

The Warwick Research Archive Portal (WRAP) makes this work by researchers of the University of Warwick available open access under the following conditions.

© 2021 Elsevier. Licensed under the Creative Commons Attribution-NonCommercial-NoDerivatives 4.0 International <http://creativecommons.org/licenses/by-nc-nd/4.0/>.



Publisher's statement:

Please refer to the repository item page, publisher's statement section, for further information.

For more information, please contact the WRAP Team at: wrap@warwick.ac.uk.

Fire testing of austenitic stainless steel I-section beam-columns

Zhe Xing^{a,b,*}, Ou Zhao^{c,*}, Merih Kucukler^d, Leroy Gardner^b

^a*College of Civil and Transportation Engineering, Hohai University, Nanjing, China*

^b*Department of Civil and Environmental Engineering, Imperial College London, London SW7 2AZ, UK*

^c*School of Civil and Environmental Engineering, Nanyang Technological University, Singapore*

^d*School of Engineering, University of Warwick, Coventry, CV4 7AL, UK*

Abstract

With the increasing use of stainless steel elements in construction, the need for comprehensive rules to enable their efficient structural design is clear. To date, the fire behaviour of stainless steel I-section beam-columns has been the subject of relatively little research. In particular, there is an absence of experimental data. To address this gap in knowledge, full-scale anisothermal fire tests on six grade 1.4301 austenitic stainless steel I-section beam-columns have been carried out; the test procedure and results are reported herein. The test specimens were subjected to eccentric axial compression with two eccentricity values so as to achieve different combinations of axial compression and uniform minor axis bending. Complementary initial local and global geometric imperfection measurements, room temperature tensile coupon tests and room temperature beam-column tests were also carried out. Based on the obtained experimental results, together with additional numerical results from a previous study, the existing design rules in the European structural steel fire design standard EN 1993-1-2 and the new design method of [1] for stainless steel beam-columns in fire, which will be incorporated into the next version of EN 1993-1-2, are assessed.

Keywords: Anisothermal; Beam-column; Experiments; Fire tests; Fire design; I-section; Laser-welded; Stainless steel

1. Introduction

Fire resistant design is a key aspect of structural engineering. Metallic structures can be vulnerable to the effects of fire, especially if unprotected, owing to their rapid temperature development, which leads to the degradation of the strength and stiffness of the material. Stainless steel, particularly the commonly used austenitic grades, exhibits better strength and stiffness retention relative to carbon steel at elevated temperatures [2–5] and is hence well suited to use in structures at risk of exposure to fire. The response of stainless steel members under compression [6–12] and bending [13, 14] in fire has been investigated in a number of previous research studies, but the

*Corresponding author

Email addresses: xingzhe@hhu.edu.cn (Zhe Xing), ou.zhao@ntu.edu.sg (Ou Zhao), merih.kucukler@warwick.ac.uk (Merih Kucukler), leroy.gardner@imperial.ac.uk (Leroy Gardner)

behaviour under combined axial compression and bending has received less attention. Lopes et al. [15, 16] conducted numerical studies into the response of stainless steel I-section, square hollow section (SHS) and circular hollow section (CHS) beam-columns in fire. Fan et al. [10] carried out two anisothermal fire tests on grade 1.4301 austenitic stainless steel square hollow section beam-columns with critical temperatures in the vicinity of 700 °C. A further series of anisothermal fire tests on rectangular hollow section beam-columns in the same stainless steel grade was reported in [17], in which three cross-section profiles, three eccentricities and a spectrum of critical temperature values ranging between 486 °C and 570 °C were considered. Thus far, however, there have been no experiments performed on stainless steel I-section beam-columns in fire.

To address the lack of experimental data on stainless steel I-section beam-columns in fire, six full-scale fire tests have been carried out on grade 1.4301 austenitic stainless steel laser-welded I-section beam-columns; the testing procedure and results are described in this paper. Two loading eccentricity values of 10 mm and 30 mm were utilised in the fire tests to achieve different combinations of axial compression and uniform minor axis bending. In addition to the fire tests, two full-scale room temperature tests on beam-columns with the same geometric properties and from the same batch of material as those of the specimens subjected to fire testing were also carried out. In the fire tests, the anisothermal testing method, which mimics a real fire situation, was adopted, whereby axial compression was first applied to the test specimens at a predefined loading eccentricity and then the specimens were heated until failure. In addition to the full-scale beam-column tests, the results of complementary room temperature tensile coupon tests and initial geometric imperfection measurements on the specimens are also reported. Finally, the accuracy and suitability of the current European fire design provisions set out in EN 1993-1-2 [18] for stainless steel I-section beam-columns, as well as new design proposals [1], are assessed against the obtained experimental results and additional existing numerical results.

2. Material properties

All tested I-section members were fabricated through the laser-welding of hot-rolled grade 1.4301 austenitic stainless steel plates, where the laser-welding was carried out to welding Class B, in line with EN ISO 13919-1 [19]. Tables 1 and 2 show the chemical composition and material properties of the tested I-section members, as provided in the manufacturer's mill certificates, where $f_{y, \text{mill}}$ is the 0.2% proof stress, $f_{p1.0, \text{mill}}$ is the 1% proof stress, $f_{u, \text{mill}}$ is the ultimate tensile stress and $\varepsilon_{f, \text{mill}}$ is the strain at fracture measured over the gauge length of $5.65 \sqrt{S_0}$, where S_0 is the cross-sectional area of the coupon. The specimen I-198×99×4.5×7 in Tables 1 and 2 refers to an I-section specimen with a nominal cross-section depth h of 198 mm, flange width b of 99 mm, web thickness t_w of 4.5 mm and flange thickness t_f of 7 mm, where h , b , t_w and t_f are also graphically illustrated in Fig. 1.

A single cross-section profile (I-198×99×4.5×7) was considered in this study. Four tensile coupons were extracted from the cross-section of the test specimen at the locations shown in Fig. 1, with two coupons cut from the web and two from the top and bottom flanges. Fig. 2 shows the dimensions of the four tensile coupons, which are in accordance with the recommendations of [20]. The tensile coupon tests were performed using a 250 kN hydraulic testing machine. Fig. 3 shows the details of the test setup, where it can be seen that an extensometer was mounted onto

the middle of the coupons and two strain gauges were adhered to the two sides of the coupons at mid-height. A displacement-controlled loading scheme was adopted in accordance with EN ISO 6892-1 [21], in which the initial loading rate was 0.05 mm/min, and once the nominal yield stress had been reached, the loading rate was increased to 0.8 mm/min until the fracture. The labelling system of the tensile coupons (TC) was based on the nominal thickness of the plate, and whether it was extracted from the web (W) or flange (F) plate of the I-section - e.g. TC4.5-W-1 indicates the tensile coupon extracted from the web of the I-section with a 4.5 mm nominal thickness. Since two specimens were extracted from both web and flange plates, an additional number at the end of the specimen label was used to differentiate between them. Figs. 4a and 4b show the measured stress-strain curves from four tensile coupons and the key material properties are reported in Table 3, where t is the coupon thickness, E is the Young's modulus, f_y is the 0.2% proof stress, $f_{p1.0}$ is the 1% proof stress, $f_{2.0}$ is the stress at 2% total strain, f_u is the ultimate tensile stress, ε_u is the ultimate strain and ε_f is the fracture strain measured over a 50 mm gauge length. The Ramberg-Osgood exponents n and m_u [22–25] in this table were obtained by fitting the two-stage compound Ramberg–Osgood material model described in [5, 24, 25] as given by eq.(1) and eq.(2), to the stress-strain curves obtained from the coupon tests. Note that $E_{p0.2}$ and $\varepsilon_{p0.2}$ in eq. (2) are the tangent modulus and total strain at the 0.2% proof stress, respectively.

$$\varepsilon = \frac{\sigma}{E} + 0.002 \left(\frac{\sigma}{f_y} \right)^n \quad \text{for } \sigma \leq f_y \quad (1)$$

$$\varepsilon = \frac{\sigma - f_y}{E_{p0.2}} + \left(\varepsilon_u - \varepsilon_{p0.2} - \frac{f_u - f_y}{E_{p0.2}} \right) \left(\frac{\sigma - f_y}{f_u - f_y} \right)^{m_u} + \varepsilon_{p0.2} \quad \text{for } f_y < \sigma \leq f_u, \quad (2)$$

3. Geometry and imperfection measurements

The geometric properties of the eight beam-column specimens were measured before conducting the tests; the measured results are reported in Table 4, where L is the buckling length of the specimens between the two centres of the knuckle bearings used in the tests, as shown in Fig. 5. The tested specimens were labelled with respect to the initial loading eccentricity e_0 , where BC-Z10 corresponds to the specimen with the initial loading eccentricity of 10 mm while BC-Z30 corresponds to the specimen with the initial loading eccentricity of 30 mm. The Z indicates that bending was induced about the minor axis, which was the case in all tests. An additional number was also utilised to signify the three different nominal axial load ratios $n_r = 0.6, 0.5$ and 0.4 applied to the specimens, which are equal to the ratios of the applied axial loading $N_{Ed, \text{test}}$ to the room temperature minor axis flexural buckling resistances N_u , determined from the room temperature beam-column tests with the corresponding loading eccentricities (i.e. $n_r = N_{Ed, \text{test}}/N_u$). Thus, BC-Z30-0.5 corresponds to the beam-column specimen with the initial loading eccentricity value of 30 mm and axial load ratio of 0.5. The beam-column specimens tested at room temperature were denoted BC-Z10-20C for the specimen with the initial loading eccentricity of 10 mm and BC-Z30-20C for the specimen with the initial loading eccentricity of 30 mm.

Initial local geometric imperfections of four beam-column specimens (BC-Z10-20C, BC-Z10-0.6, BC-Z30-20C and BC-Z30-0.6) and initial global geometric imperfections of all beam-column

specimens were measured in line with the procedure adopted by Schafer and Peköz [26–28]. For the local imperfection measurements, the specimens were first secured to the bed of a CNC milling machine, and then an LVDT, which was attached to the movable frame of the CNC milling machine, was moved along a 600 mm length away from the ends of the specimens to record displacements at 1 mm intervals, as shown in Fig. 6; lines of measurements were taken at the nine different locations illustrated in Fig. 7. A typical measured local geometric imperfection distribution is shown in Fig. 8a. The measured web local geometric imperfection magnitudes w_w and flange local geometric imperfection magnitudes w_f , which are summarised in Table 4, were defined as the maximum deviations from a straight line fitted to the local imperfection measurements along the specimen lengths using least squares regression. As can be seen from Table 4, the measured web w_w and flange w_f local geometric imperfection magnitudes are significantly lower than the manufacturing tolerance of 1/100 of the web height and 1/100 of the flange width set out in EN 1090-2 [29].

When measuring the initial global geometric imperfection magnitudes, the LVDT, attached to the movable frame of the CNC milling machine, recorded the deviations at Point 5 on the cross-sections (see Fig. 7) along the full lengths L_s of the specimens with the exception of two 100 mm portions at the ends of the specimens due to the limited maximum range of the movable frame of the CNC milling machine. Fig. 8b shows a typical measured initial global geometric imperfection distribution where the maximum deviation from a straight line connecting the ends of the measured length of the specimen was taken as the maximum global geometric imperfection v_0 . The measured global geometric imperfections v_0 are summarized in Table 4, where it can be seen that the measured global geometric imperfections v_0 are significantly lower than the manufacturing tolerance of $L_s/1000$ set out in EN 1090-2 [29].

4. Beam-column tests at room temperature

To obtain reference resistances for the fire tests to be benchmarked against, two corresponding specimens were tested under combined axial compression and minor axis bending at room temperature. The specimens had the same nominal cross-section size of I-198×99×4.5×7 and the same nominal buckling length L of 2.75 m. Two values of initial loading eccentricities e_0 equal to 10 mm and 30 mm were considered to achieve different bending moment-to-axial load ratios. As shown in Fig. 9, the initial loading eccentricity e_0 was introduced by eccentrically welding the specimens to the end plates; the distance between the centrelines of the end plate and the specimen was equal to the initial loading eccentricity e_0 .

4.1. Test setup and procedures

Fig. 5 shows the overall experimental setup used in the room temperature beam-column tests, which consisted of a 5000 kN capacity horizontal self-reacting test rig with a hydraulic actuator to apply the axial load, knuckle bearings at the two ends of the test specimens to provide pin-ended support conditions about minor axis, four LVDTs placed at four corners of the right hand end plate to measure the end rotations and one string transducer attached to the middle of the specimens to measure the mid-height lateral deflections. Lubricating oil was applied to reduce friction in the pins of the supports during testing. The furnace was retained in situ but left open during the room

temperature testing. Fig. 10 shows the details of the loading system at the left hand end of the setup, where a load cell was placed between the actuator and the left hand knuckle bearing to measure the load applied by the actuator. Before testing, a laser level was utilised to ensure that the actuator, the load cell and the pins of two knuckle bearings were aligned.

The total test eccentricity comprised the initial loading eccentricity e_0 and the global imperfection of the test specimens v_0 . To measure the total test eccentricity ($e_0 + v_0$), four strain gauges were affixed to the specimens at mid-height at a distance of $d_s = 10$ mm from the outer edges of the four flanges, according to the method described in [30, 31]. The calculation of the total eccentricity ($e_0 + v_0$) was performed using eqs. (3)–(5):

$$e_0 + v_0 = \frac{EI_z(\varepsilon_{\max} - \varepsilon_{\min})}{N(b_f - 2d_s)} - \delta, \quad (3)$$

in which

$$\varepsilon_{\max} = (\varepsilon_1 + \varepsilon_2)/2, \quad (4)$$

$$\varepsilon_{\min} = (\varepsilon_3 + \varepsilon_4)/2, \quad (5)$$

where $\varepsilon_1, \varepsilon_2, \varepsilon_3$ and ε_4 are the strain gauge readings, E is the modulus of elasticity, I_z is the minor axis second moment of area, N is the applied load and δ is the mid-height lateral deflection. The locations of the four strain gauges are illustrated in Fig. 11. The measured total test eccentricities are summarised in Table 5. In the room temperature beam-column tests, a displacement-controlled loading scheme was applied with a constant rate of 0.3 mm/min. All the data, including the applied load, the mid-height lateral deflection, the strain values measured by the four strain gauges at mid-height and the displacements measured by the four LVDTs, were recorded by a data logger at 1 s intervals.

4.2. Test results

The two tested beam-column specimens (BC-Z10-20C and BC-Z30-20C) failed by flexural buckling about the minor axis, which was accentuated by the presence of the applied minor axis bending moment. A typical failure mode of the tested beam-columns, that of BC-Z30-20C, is shown in Fig. 12. The load versus mid-height lateral displacement curves for the two beam-column tests are plotted in Fig. 13. The key results from these two beam-column tests are summarised in Table 5, where M_u is the first order ultimate bending moment, calculated as:

$$M_u = N_u(v_0 + e_0). \quad (6)$$

5. Beam-column fire tests

Six fire tests on pin-ended stainless steel I-section beam-columns under combined axial compression and bending about the minor axis were carried out in this study. The cross-section of the six beam-column specimens was an I-198×99×4.5×7 profile and the buckling length of members

was equal to 2.75 m, mirroring two beam-columns tested at room temperature. Of the six beam-column fire tests, three tests were conducted with an initial nominal loading eccentricity e_0 of 10 mm and three were carried out with an initial nominal loading eccentricity e_0 of 30 mm. All the beam-column fire tests were carried out anisothermally. Anisothermal testing is considered to be more representative of a real fire situation than isothermal testing, where the specimens are heated up to the target temperature and then loaded until failure [4, 32]. Three different load ratios n_r , equal to 0.6, 0.5 and 0.4, were adopted to achieve a range of failure temperatures.

5.1. Test setup

Fig. 14 shows the beam-column fire test setup, which consisted of a 5000 kN capacity horizontal self-reacting test rig with a hydraulic actuator, an electric furnace, an LVDT with a bespoke displacement measurement system to measure the mid-height lateral deflection of the specimen and four strain gauges to derive the total test eccentricity. Note that the fire test specimens were uniformly heated along their length, except for 240 mm at each end. These end regions were located outside the furnace and were therefore not directly heated; this was because the knuckle bearings connected to the end plates of the specimens had to be placed outside the furnace and required space to rotate. Before testing, the left hand and right hand openings of the furnace were heavily insulated around the specimen by heat resistant fabric and rockwool to limit any heat loss.

The electric furnace shown in Fig. 15 was used in the beam-column fire tests. During testing, the air temperature of the furnace, which was measured through two thermocouples, was increased in accordance with the ISO-834 standard fire curve [33], as shown in Fig. 16. One of the thermocouples was connected to the furnace heating control system and the other thermocouple was embedded in a furnace wall (see Fig. 17). In addition to these two thermocouples, there were seven thermocouples attached to the specimens at a series of points along their lengths to capture the surface temperature distribution; the locations of the thermocouples are illustrated in Fig. 18, where thermocouple 1 and 7 were used for measuring the temperature of the two ends of the specimens that lay outside the furnace.

Fig. 19 shows the LVDT used to measure the mid-height lateral deflection of the beam-column specimens; the LVDT was installed above the furnace and covered with heat resistant fabric. The uncovered extension rod of the LVDT was connected to the bespoke displacement measurement system shown in Fig. 15 using an Alsint 99.7 rod. Alsint 99.7 has a high yield strength (300 MPa) and a low coefficient of thermal expansion ($7.8 \times 10^{-6} \text{ K}^{-1}$). The Alsint 99.7 rod, one end of which was connected to the extension rod of the LVDT and the other end of which was attached to the surface of the specimen, was able to move vertically with the extension rod of the LVDT to measure the lateral deflection of the specimens at the mid-height.

5.2. Testing procedure

In the beam-column fire tests, a predefined compressive load $N_{\text{Ed,test}}$ at a predetermined eccentricity was first applied to the specimens under displacement control at a rate of 0.3 mm/min. Once the predefined load ratio $n_r = N_{\text{Ed,test}}/N_u$, where $N_{\text{Ed,test}}$ is the applied compressive load and N_u is the compressive load at failure of the equivalent beam-column at room temperature, as determined in Section 4, has been reached, the testing was switched to load control and the load was held constant for fifteen minutes. The air temperature of the furnace was then increased following the

ISO-834 standard fire curve [33] until the test load $N_{\text{Ed,test}}$ could no longer be sustained. During the heating process, the specimen was allowed to expand to keep the predefined axial compression load $N_{\text{Ed,test}}$ constant. The pre-applied compressive load $N_{\text{Ed,test}}$, load ratios n_r and the measured total eccentricity ($e_0 + v_0$) of the six beam-column tests are reported in Table 6.

5.3. Test results

As anticipated, all the tested beam-column specimens failed by flexural buckling about the minor axis accentuated by the presence of minor axis bending. Fig. 20 shows the failure modes of the beam-column specimens with the 10 mm nominal eccentricity for the three different load ratios n_r . The specimens with the 30 mm nominal eccentricity exhibited similar failure modes. In this subsection, additional details are presented regarding the temperature distributions and the behaviour of the specimens observed during the testing.

5.3.1. Temperature distributions

The measured air temperature versus time relationships for the six beam-column fire tests are shown in Fig. 21a–21b, together with the ISO-834 standard fire curve [33]. As can be seen from the figures, the air temperature in the furnace generally followed the trend of the ISO-834 standard fire curve [33] though lagged somewhat behind, particularly at the beginning of the experiments.

Fig. 22 shows the temperature values measured by the seven thermocouples attached to the surface of the specimens. In this figure, the temperatures measured by thermocouples 2–6 in the heated region can be seen to have increased following a similar trend with time. The temperatures of the two unheated parts outside the furnace were measured by thermocouple 1 and thermocouple 7 found to remain at room temperature throughout the testing. Figs. 23a and 23b show the average measured surface temperature-time relationships for all six fire test specimens, where the surface temperatures are taken as the mean temperature values measured by the five thermocouples attached to the specimens in the heated regions. The key experimental results from the six beam-column fire tests are summarised in Table 7, including the critical failure temperature θ_{cr} and the fire resistance in terms of duration $t_{\text{fi,test}}$ for which the specimens were able to resist the pre-applied loads $N_{\text{Ed,test}}$. The fire resistances $t_{\text{fi,test}}$ and critical temperatures $\theta_{\text{cr,test}}$ were defined based on the point at which either one of the two failure criteria provided in the European Standard EN 1363-1 (2012) [34] was reached: (i) the maximum allowable axial contraction magnitude of $C = h/100$ mm or (ii) the maximum allowable axial contraction rate of $dC/dt = 3h/1000$ mm/min, where h is the initial specimen height in mm.

5.3.2. Behaviour of specimens

The axial deformation versus temperature paths for the tested six stainless steel beam-column specimens are shown in Fig. 24. It can be seen that the beam-column specimens shortened initially due to the pre-applied load ($N_{\text{Ed,test}}$ and, due to the eccentricity, $M_{\text{Ed,test}}$), and then started to expand with increasing temperatures. When the beam-column specimen temperatures were below about 300 °C, it can be seen in Fig. 24 that the measured axial expansion rates of the specimens were smaller than those measured for high temperature levels. This was mainly because the specimen temperatures increased rapidly to 300 °C and the position of the actuator, which was manually controlled to maintain a constant axial loading, lagged slightly behind where it ought to have been.

After reaching 300 °C, the specimen temperature increased more slowly and all the specimens expanded linearly with increasing temperature values until failure.

Fig. 25 shows the mid-height lateral deflection versus average surface temperature paths for the six fire test specimens, where the thermal expansion of the Alsint 99.7 rod (up to about 3 mm at 800 °C) has been removed from the measured mid-height lateral deflections of the beam-column specimens. As shown in Fig. 25, there was a small mid-height lateral deflection under the initial applied load; as the beam-column specimens approached failure, their stiffness reduced rapidly and there were significant increases in mid-height lateral deflections, signifying flexural buckling about the minor axis. It also can be observed in this figure that, although the specimen BC-Z30-0.5 was tested under a lower load ratio relative to BC-Z30-0.6, the lateral deflection of BC-Z30-0.5 was higher than that of BC-Z30-0.6 in the temperature range from 20 °C to 400 °C. This relates to the rapid expansion problem described above, which was more pronounced (i.e. belatedly rectified) in the first conducted test (BC-Z30-0.5), and lead to enhanced lateral deflections. The problem was largely resolved in the subsequent tests by making more frequent but smaller changes to the actuator position, and is not considered to affect the overall outcome of the tests.

6. Assessment of design rules for stainless steel I-section beam-columns in fire

In this section, the EN 1993-1-2 beam-column design rules [18] and the new beam-column design method of Kucukler et al. [1], which is due to be incorporated into the upcoming revision of EN 1993-1-2 [18], are presented and assessed. To supplement the rather limited number of experimental results generated herein, existing numerical results [1], covering three different cross-section profiles (IPE 100, IPE 200 and IPE 300), three global slenderness values ($\bar{\lambda}_\theta = 0.5, 1.0$ and 1.5) and four different elevated temperature levels, are also utilized in the comparisons. Further analysis, confirming the accuracy of the new design method [1], has been presented in [1]; the accuracy of the new stainless steel design rules has also been demonstrated by Martins et al. [35].

Their ultimate strength predictions of stainless steel beam-columns in fire are determined using the design method $N_{u,pred}$ at the corresponding measured failure temperatures θ_{cr} and then compared with the experimental results $N_{u,pred}$ obtained in the previous section. If the ratio of N_u to $N_{u,pred}$ is greater than or equal to unity, the resistance predicted by the design method $N_{u,pred}$ is on the safe side. The predicted resistances $N_{u,pred}$ were obtained assuming proportional loading, following a similar approach to that reported in [31, 36, 37], as shown in Fig. 26, where a single parameter θ , referred to as the radial angle, is introduced to describe the combination of axial load and bending moment, which is calculated as:

$$\theta = \tan^{-1} \left(\frac{N/N_{Rd}}{M/M_{Rd}} \right), \quad (7)$$

where N_{Rd} and M_{Rd} are the axial compression resistance and bending moment resistance predicted by the design method, respectively. The value of $N_{u,pred}/N_{Rd}$ therefore corresponds to the vertical distance from the origin to the intersection with the design interaction curve. Additionally, as can be seen from the Fig. 26, when the radial angle θ increases from 0° to 90°, the applied loading changes from pure bending ($\theta = 0^\circ$) to combined axial compression and bending ($0^\circ < \theta < 90^\circ$), and then to pure compression ($\theta = 90^\circ$).

It should be noted that the elevated temperature material properties of stainless steel (i.e. $f_{p0.2,\theta}$, $f_{2,\theta}$, E_θ , $f_{u,\theta}$ and $\varepsilon_{u,\theta}$) used in the design methods presented in this section can be estimated by multiplying the strength ($k_{p0.2,\theta}$, $k_{2,\theta}$), stiffness ($k_{E,\theta}$) and ductility ($k_{\varepsilon_{u,\theta}}$) reduction factors given in [38] (see Fig. 27), which are based on the results of extensive material testing [39–41], by the corresponding room temperature material properties, i.e. $f_{p0.2,\theta} = k_{p0.2,\theta}f_y$, $f_{2,\theta} = k_{2,\theta}f_y$, $E_\theta = k_{E,\theta}E$, $f_{u,\theta} = k_{u,\theta}f_u$ and $\varepsilon_{u,\theta} = k_{\varepsilon_{u,\theta}}\varepsilon_u$, where $f_{p0.2,\theta}$ is the 0.2% proof strength at temperature θ , E_θ is the modulus of elasticity at temperature θ and $f_{u,\theta}$ and $\varepsilon_{u,\theta}$ are the ultimate tensile strength and strain at temperature θ .

6.1. EN 1993-1-2 design rules [18]

EN 1993-1-2 [18] states that a member subjected to combined axial compression and bending in fire should satisfy expressions (8)–(9) when it has a Class 1 or Class 2 cross-section:

$$\frac{N_{fi,Ed}}{\chi_{min,fi} A k_{y,\theta} \frac{f_y}{\gamma_{M,fi}}} + \frac{k_y M_{y,fi,Ed}}{W_{pl,y} k_{y,\theta} \frac{f_y}{\gamma_{M,fi}}} + \frac{k_z M_{z,fi,Ed}}{W_{pl,z} k_{y,\theta} \frac{f_y}{\gamma_{M,fi}}} \leq 1, \quad (8)$$

$$\frac{N_{fi,Ed}}{\chi_{z,fi} A k_{y,\theta} \frac{f_y}{\gamma_{M,fi}}} + \frac{k_{LT} M_{y,fi,Ed}}{\chi_{LT,fi} W_{pl,y} k_{y,\theta} \frac{f_y}{\gamma_{M,fi}}} + \frac{k_z M_{z,fi,Ed}}{W_{pl,z} k_{y,\theta} \frac{f_y}{\gamma_{M,fi}}} \leq 1, \quad (9)$$

expressions (10)–(11) when it has a Class 3 cross-section:

$$\frac{N_{fi,Ed}}{\chi_{min,fi} A k_{y,\theta} \frac{f_y}{\gamma_{M,fi}}} + \frac{k_y M_{y,fi,Ed}}{W_{el,y} k_{y,\theta} \frac{f_y}{\gamma_{M,fi}}} + \frac{k_z M_{z,fi,Ed}}{W_{el,z} k_{y,\theta} \frac{f_y}{\gamma_{M,fi}}} \leq 1, \quad (10)$$

$$\frac{N_{fi,Ed}}{\chi_{z,fi} A k_{y,\theta} \frac{f_y}{\gamma_{M,fi}}} + \frac{k_{LT} M_{y,fi,Ed}}{\chi_{LT,fi} W_{el,y} k_{y,\theta} \frac{f_y}{\gamma_{M,fi}}} + \frac{k_z M_{z,fi,Ed}}{W_{el,z} k_{y,\theta} \frac{f_y}{\gamma_{M,fi}}} \leq 1, \quad (11)$$

and expressions (12)–(13) when it has a Class 4 cross-section:

$$\frac{N_{fi,Ed}}{\chi_{min,fi} A_{eff} k_{y,\theta} \frac{f_y}{\gamma_{M,fi}}} + \frac{k_y M_{y,fi,Ed}}{W_{eff,y} k_{y,\theta} \frac{f_y}{\gamma_{M,fi}}} + \frac{k_z M_{z,fi,Ed}}{W_{eff,z} k_{y,\theta} \frac{f_y}{\gamma_{M,fi}}} \leq 1, \quad (12)$$

$$\frac{N_{fi,Ed}}{\chi_{z,fi} A_{eff} k_{y,\theta} \frac{f_y}{\gamma_{M,fi}}} + \frac{k_{LT} M_{y,fi,Ed}}{\chi_{LT,fi} W_{eff,y} k_{y,\theta} \frac{f_y}{\gamma_{M,fi}}} + \frac{k_z M_{z,fi,Ed}}{W_{eff,z} k_{y,\theta} \frac{f_y}{\gamma_{M,fi}}} \leq 1. \quad (13)$$

In eqs. (8)–(13), $N_{fi,Ed}$ is the design axial force, $M_{y,fi,Ed}$ and $M_{z,fi,Ed}$ are the maximum major and minor axes first order bending moments, $\chi_{min,fi}$ is the lowest of the buckling reduction factors determined for flexural buckling about the major and minor axes, torsional buckling and torsional-flexural buckling, $\chi_{z,fi}$ is the lowest of the buckling reduction factors determined for flexural buckling about the minor axis, torsional buckling and torsional-flexural buckling and $\chi_{LT,fi}$ is the reduction factor for lateral-torsional buckling. Additionally, A and A_{eff} are the gross cross-sectional area and the effective area, $W_{pl,y}$, $W_{el,y}$ and $W_{eff,y}$ are the plastic, elastic and effective section moduli about the major axis respectively, $W_{pl,z}$, $W_{el,z}$ and $W_{eff,z}$ are the plastic, elastic and effective section moduli about the minor axis respectively, $k_{y,\theta}$ is the yield strength reduction factor taken as $k_{2,\theta}$ for members with Class 1, 2 or 3 cross-sections and $k_{p0.2,\theta}$ for members with Class 4 cross-sections, f_y is the yield strength (i.e. 0.2% proof strength) at room temperature, $\gamma_{M,fi}$ is the partial safety factor for fire design taken as 1.0 and k_y , k_z and k_{LT} are the interaction coefficients calculated as:

$$k_y = 1 - \frac{\mu_y N_{fi,Ed}}{\chi_{y,fi} A k_{y,\theta} \frac{f_y}{\gamma_{M,fi}}} \leq 3 \quad (14)$$

with $\mu_y = (2\beta_{M,y} - 5)\bar{\lambda}_{y,\theta} + 0.44\beta_{M,y} + 0.29 \leq 0.8$,

$$k_z = 1 - \frac{\mu_z N_{fi,Ed}}{\chi_{z,fi} A k_{y,\theta} \frac{f_y}{\gamma_{M,fi}}} \leq 3 \quad (15)$$

with $\mu_z = (1.2\beta_{M,z} - 3)\bar{\lambda}_{z,\theta} + 0.71\beta_{M,z} - 0.29 \leq 0.8$, and

$$k_{LT} = 1 - \frac{\mu_{LT} N_{fi,Ed}}{\chi_{z,fi} A k_{y,\theta} \frac{f_y}{\gamma_{M,fi}}} \leq 1 \quad (16)$$

with $\mu_{LT} = 0.15\bar{\lambda}_{z,\theta}\beta_{M,LT} - 0.15 \leq 0.9$, where $\beta_{M,y}$ and $\beta_{M,z}$ are the equivalent uniform moment factors. Comparisons of the pre-applied axial compression loads $N_{Ed,test}$ in the fire tests and the Eurocode 3 Part 1.2 capacity predictions for compression plus minor axis bending $N_{b,Rd,EC3}$, determined at the measured critical temperature θ_{cr} values for each test specimen, are shown in Table 8. Note that the minor axis bending moments $M_{z,fi,Ed}$ were determined by multiplying the applied axial load $N_{fi,Ed}$ by the corresponding initial eccentricity values. The assessment of the EN 1993-1-2 [18] design rules based on the test results generated herein and the existing numerical results is shown in Fig. 28a. As can be seen from the figure, a large number of the $N_{Ed}/N_{Ed,EC3}$ ratios are lower than 1.0, which indicates that the EN 1993-1-2 [18] design rules lead to ultimate strength predictions that lie generally on the unsafe side for austenitic stainless steel I-section beam-columns in fire.

6.2. New design method proposed by Kucukler et al. [1]

In the new design method of Kucukler et al. [1], cross-sections are classified into two classes – ‘non-slender’ and ‘slender’ – in line with the cross-section classification approach reported in [42].

The design buckling resistance of a member subject to combined axial compression and bending in fire should satisfy expressions (17)–(18) when it has a non-slender cross-section:

$$\frac{N_{fi,Ed}}{\chi_{y,fi} A k_{2,\theta} \frac{f_y}{\gamma_{M,fi}}} + k_{yy} \frac{M_{y,fi,Ed}}{W_{pl,y} k_{2,\theta} \frac{f_y}{\gamma_{M,fi}}} + k_{yz} \frac{M_{z,fi,Ed}}{W_{pl,z} k_{2,\theta} \frac{f_y}{\gamma_{M,fi}}} \leq 1, \quad (17)$$

$$\frac{N_{fi,Ed}}{\chi_{z,fi} A k_{2,\theta} \frac{f_y}{\gamma_{M,fi}}} + k_{zy} \frac{M_{y,fi,Ed}}{\chi_{LT,fi} W_{pl,y} k_{2,\theta} \frac{f_y}{\gamma_{M,fi}}} + k_{zz} \frac{M_{z,fi,Ed}}{W_{pl,z} k_{2,\theta} \frac{f_y}{\gamma_{M,fi}}} \leq 1, \quad (18)$$

or expressions (19)–(20) when it has a slender cross-section:

$$\frac{N_{fi,Ed}}{\chi_{y,fi} A_{eff} k_{2,\theta} \frac{f_y}{\gamma_{M,fi}}} + k_{yy} \frac{M_{y,fi,Ed} + \Delta M_{y,fi,Ed}}{W_{eff,y} k_{2,\theta} \frac{f_y}{\gamma_{M,fi}}} + k_{yz} \frac{M_{z,fi,Ed} + \Delta M_{z,fi,Ed}}{W_{eff,z} k_{2,\theta} \frac{f_y}{\gamma_{M,fi}}} \leq 1, \quad (19)$$

$$\frac{N_{fi,Ed}}{\chi_{z,fi} A_{eff} k_{2,\theta} \frac{f_y}{\gamma_{M,fi}}} + k_{zy} \frac{M_{y,fi,Ed} + \Delta M_{y,fi,Ed}}{\chi_{LT,fi} W_{eff,y} k_{2,\theta} \frac{f_y}{\gamma_{M,fi}}} + k_{zz} \frac{M_{z,fi,Ed} + \Delta M_{z,fi,Ed}}{W_{eff,z} k_{2,\theta} \frac{f_y}{\gamma_{M,fi}}} \leq 1, \quad (20)$$

where $\Delta M_{y,fi,Ed}$ and $\Delta M_{z,fi,Ed}$ are the moments due to the shift of the centroidal axes, $\chi_{y,fi}$ is the buckling reduction factor for flexural buckling about the major axis, $\chi_{z,fi}$ is the minimum of the buckling reduction factors for minor axis flexural buckling, torsional or torsional-flexural buckling and $\chi_{LT,fi}$ is the buckling reduction factor for lateral-torsional buckling; the determination of $\chi_{y,fi}$ and $\chi_{z,fi}$ using the newly derived column buckling curves for stainless steel members in fire is described in [43]. The buckling reduction factor for lateral-torsional buckling $\chi_{LT,fi}$ in eq. (18) and eq. (20) is calculated as:

$$\chi_{LT,fi} = \frac{1}{\phi_{LT,\theta,com} + \sqrt{\phi_{LT,\theta,com}^2 - \bar{\lambda}_{LT,\theta,com}^2}} \quad \text{but} \quad \chi_{LT,fi} \leq 1, \quad (21)$$

and

$$\phi_{LT,\theta,com} = 0.5 \left[1 + \eta_{LT,\theta}^* + \bar{\lambda}_{LT,\theta,com}^2 \right], \quad (22)$$

where

$$\eta_{LT,\theta}^* = \alpha_{LT} \bar{\lambda}_{LT,\theta,com}, \quad (23)$$

in which α_{LT} is the elevated temperature imperfection factor for lateral-torsional buckling expressed as:

$$\alpha_{LT} = \alpha_{LT,0} / \xi_{\theta}. \quad (24)$$

The non-dimensional slenderness $\bar{\lambda}_{LT,\theta,com}$ is determined by:

$$\bar{\lambda}_{LT,\theta,com} = \sqrt{\frac{W_{pl,y} k_{2,\theta} f_y}{M_{cr,\theta}}} \quad \text{for non-slender sections,} \quad (25)$$

$$\bar{\lambda}_{LT,\theta,com} = \sqrt{\frac{W_{eff,y} k_{2,\theta} f_y}{M_{cr,\theta}}} \quad \text{for slender sections.} \quad (26)$$

Note that in eq. (26), $W_{eff,y}$ is determined through the effective width design method put forward by Xing et al. [42]. The parameters k_{yy} , k_{yz} , k_{zy} and k_{zz} in eqs. (17)–(20) are interaction factors for the design of members with doubly symmetric cross-sections. For cases in which member instability is governed by the buckling about the major axis, the interaction factor k_{yy} is calculated as:

$$k_{yy} = C_{my} \left[1 + D_{1,y} (\bar{\lambda}_{y,\theta} - D_{2,y}) n_y \right] \quad \text{for } \bar{\lambda}_{y,\theta} < D_{3,y}, \quad (27)$$

$$k_{yy} = C_{my} \left[1 + D_{1,y} (D_{1,y} - D_{3,y}) n_y \right] \quad \text{for } \bar{\lambda}_{y,\theta} \geq D_{3,y}, \quad (28)$$

and the interaction factor k_{yz} is taken as:

$$k_{yz} = C_{mz} \left[1 + D_{1,z} (\bar{\lambda}_{z,\theta} - D_{2,z}) n_z \right] \quad \text{for } \bar{\lambda}_{z,\theta} < D_{3,z}, \quad (29)$$

$$k_{yz} = C_{mz} \left[1 + D_{1,z} (D_{3,z} - D_{2,z}) n_z \right] \quad \text{for } \bar{\lambda}_{z,\theta} \geq D_{3,z}, \quad (30)$$

in which the parameters n_y and n_z are given by:

$$n_y = \frac{N_{fi,Ed}}{\chi_{y,fi} A k_{2,\theta} \frac{f_y}{\gamma_{M,fi}}} \quad \text{and} \quad n_z = \frac{N_{fi,Ed}}{\chi_{z,fi} A k_{2,\theta} \frac{f_y}{\gamma_{M,fi}}} \quad \text{for non-slender sections,} \quad (31)$$

$$n_y = \frac{N_{fi,Ed}}{\chi_{y,fi} A_{eff} k_{2,\theta} \frac{f_y}{\gamma_{M,fi}}} \quad \text{and} \quad n_z = \frac{N_{fi,Ed}}{\chi_{z,fi} A_{eff} k_{2,\theta} \frac{f_y}{\gamma_{M,fi}}} \quad \text{for slender sections.} \quad (32)$$

For cases in which member instability is governed by the buckling about the minor axis, the interaction factor k_{zy} is taken as $0.8k_{yy}$ for members not susceptible to lateral-torsional buckling, while the interaction factor k_{zy} is calculated as:

$$k_{zy} = 1 - \frac{D_{1,LT} \bar{\lambda}_{z,\theta} N_z}{C_{mLT} - D_{2,LT}} \quad \text{for } \bar{\lambda}_{z,\theta} < D_{3,LT}, \quad (33)$$

$$k_{zy} = 1 - \frac{D_{1,LT} D_{3,LT} N_z}{C_{mLT} - D_{2,LT}} \quad \text{for } \bar{\lambda}_{z,\theta} \geq D_{3,LT}, \quad (34)$$

for members susceptible to lateral-torsional buckling; k_{zz} is equal to k_{yz} , as defined in eqs. (29)–(30). D_y and D_z in eqs. (27)–(30) and D_{LT} in eqs. (33)–(34) are auxiliary coefficients that are dependent on the cross-section type and stainless steel grade. For the austenitic stainless steel I-sections tested in this study, $D_{1,z}$, $D_{2,z}$ and $D_{3,z}$ are 3.0, 0.2 and 1.4, respectively [1]. The factors C_{my} and C_{mz} in eqs. (27)–(30) and C_{mLT} in eqs. (33)–(34) are the equivalent uniform moment factors defined in prEN 1993-1-1, which are taken as 1.0 in the case of a uniform bending moment distribution. The effective section properties A_{eff} and $W_{y,eff}$ within eqs. (19) and (20) are determined using the effective width method put forward by Xing et al. [42], while $W_{z,eff}$ within eqs. (19) and (20) is determined using the plastic effective width method described in Bambach and Rasmussen [44], but with the elevated temperature plate buckling slenderness $\bar{\lambda}_{p,\theta}$ defined in [42]. The heating rate and hence the effects of creep are not explicitly considered either within the general Eurocode 3 structural fire design framework [1] or the proposed design method set out in [18], and have not been examined in the present study. The effect of creep does however inherently feature in the material property elevated temperature reduction factors provided for structural fire design [1, 45–47]. The heating rates employed in the studies conducted to determine the elevated temperature material properties for stainless steel were typically around 5 to 10 °C/min [39]; this rate is considered to be broadly representative of that experienced by a structural member in a fire [48], though this would of course depend the real fire conditions, the location of the material, the presence of fire protection and other factors. The member tests performed herein followed the standard fire curve, which is used to enable a direct comparison between the fire performance of components.

Table 9 provides a comparison between the pre-applied compressive loads $N_{Ed,test}$ in the fire tests and the predicted compressive load $N_{b,Rd,Prop}$ using the design method of [1], with effective section properties from [42, 44], for members with the test eccentricity and at the corresponding measured critical temperature values θ_{cr} . As can be seen from this table, all ratios of $N_{Ed,test}$ to $N_{b,Rd,Prop}$ are higher than unity, showing that the beam-column design method proposed by Kucukler et al. [1] provides safe-sided resistance predictions for the tested members. The assessment of the design method of [1] based on the experimental and numerical results is also shown in Fig. 28b, where it can be seen that, compared to EN 1993-1-2 [18], the design method of [1] leads to more accurate and considerably less scattered ultimate strength predictions for austenitic stainless steel beam-columns in fire. It should be noted that, with the use of $k_{2,\theta}$, a higher proportion of cross-sections fall into the slender category [42], for which effective section properties are used. Therefore, even though a higher material strength is used in the design method of Kucukler et al. [1] relative to EN 1993-1-2 [18], when coupled with the reduced cross-section properties, consistent and safe-sided resistance predictions are achieved.

7. Conclusions

An experimental study of grade 1.4301 austenitic stainless steel laser-welded I-section beam-columns in fire has been presented. Material properties at room temperature were obtained by testing tensile coupons extracted from the web and flange plates of the stainless steel specimens; the corresponding elevated temperature material properties were inferred on the basis of the strength and stiffness reduction factors set out in [38–40]. Before the fire tests, two beam-column speci-

mens with the same geometrical properties as those subjected to fire testing were tested at room temperature to obtain benchmark room temperature failure loads N_u . Six anisothermal fire tests were then conducted on stainless steel I-section beam-columns. In the fire tests, two initial loading eccentricity values e_0 , equal to 10 mm and 30 mm, and three load ratios n_r , equal to 0.4, 0.5 and 0.6, were employed to achieve a range of bending moment-to-axial load ratios and a range of failure temperatures. The beam-column fire design methods provided in the current version of EN 1993-1-2 [18] and in [1] were assessed against the obtained experimental results and additional numerical results from [1], indicating that the predictions of the beam-column design method of Kucukler et al. [1] are safe and accurate. The range of applicability of the design method, in terms of heating rate, depends largely on the input material properties. The design formulae examined herein, utilising the material property reduction factors provided in [1], are considered to be applicable to the range of heating rates typically experienced in structures in fire. The obtained experimental data in this paper addresses an important gap in experimental knowledge on the fire behaviour of stainless steel I-section beam-columns and, together with the numerical results, provides additional validation of the suitability of the beam-column design method of Kucukler et al. [1] for inclusion into the next revision of EN 1993-1-2.

Acknowledgement

The authors would like to thank Stainless Structural Asia and Montanstahl AG for providing the laser-welded stainless steel I-section beam-column specimens for the project. The contributions of Toh Yau Meng, Cheng Weng Kong, Li Fali, Choi Siew Pheng and Lim Yong Cheng from the Construction Technology Laboratory at Nanyang Technological University are gratefully acknowledged.

References

- [1] Kucukler, M., Xing, Z. and Gardner, L.. Stability of stainless steel I-section beam-columns at elevated temperatures. *International Journal of Structural Stability and Dynamics* 2021;21:3.
- [2] Baddoo, N.R. and Burgan, B.A.. Fire resistant design of austenitic structural stainless steel. *Journal of Constructional Steel Research* 1998;1(46):458–459.
- [3] Gardner, L. and Ng, K.T.. Temperature development in structural stainless steel sections exposed to fire. *Fire Safety Journal* 2006;41(3):185–203.
- [4] Gardner, L. and Baddoo, N.. Fire testing and design of stainless steel structures. *Journal of Constructional Steel Research* 2006;62:532–543.
- [5] Gardner, L.. Stability and design of stainless steel structures – Review and outlook. *Thin-Walled Structures* 2019;141:208–216.
- [6] Uppfeldt, B., Ala-Outinen, T. and Veljkovic, M.. A design model for stainless steel box columns in fire. *Journal of Constructional Steel Research* 2008;64(11):1294–1301.
- [7] To, E.C.Y. and Young, B.. Performance of cold-formed stainless steel tubular columns at elevated temperatures. *Engineering Structures* 2008;30(7):2012–2021.
- [8] Lopes, N., Vila-Real, P., da Silva, L. and Franssen, J.M.. Axially loaded stainless steel columns in case of fire. *Journal of Structural Fire Engineering* 2010;1(1):43–60.
- [9] Tondini, N., Rossi, B. and Franssen, J.M.. Experimental investigation on ferritic stainless steel columns in fire. *Fire Safety Journal* 2013;62:238–248.
- [10] Fan, S., Ding, X., Sun, W., Zhang, L. and Liu, M.. Experimental investigation on fire resistance of stainless steel columns with square hollow section. *Thin-Walled Structures* 2016;98:196–211.

- [11] Ding, R., Fan, S., Chen, G., Li, C., Du, E. and Liu, C.. Fire resistance design method for restrained stainless steel H-section columns under axial compression. *Fire Safety Journal* 2019;108,102837.
- [12] Mohammed, A. and Afshan, S.. Numerical modelling and fire design of stainless steel hollow section columns. *Thin-Walled Structures* 2019;144,106243.
- [13] Ng, K.T. and Gardner, L.. Buckling of stainless steel columns and beams in fire. *Engineering Structures* 2007;29(5):717–730.
- [14] Vila-Real, P., Lopes, N., da Silva, L.S. and Franssen, J.M.. Lateral-torsional buckling of stainless steel I-beams in case of fire. *Journal of Constructional Steel Research* 2008;64(11):1302–1309.
- [15] Lopes, N., Vila-Real, P., da Silva, L.S. and Franssen, J.M.. Numerical analysis of stainless steel beam-columns in case of fire. *Fire Safety Journal* 2012;50:35–50.
- [16] Lopes, N., Manuel, M., Sousa, A.R. and Vila-Real, P.. Parametric study on austenitic stainless steel beam-columns with hollow sections under fire. *Journal of Constructional Steel Research* 2019;152:274–283.
- [17] Fan, S., Liu, M., Sun, W., Guo, Y. and Han, Y. L.. Experimental investigation of eccentrically compressed stainless steel columns with constraints in fire. *Fire Safety Journal* 2018;99:49–62.
- [18] EN 1993-1-2, Eurocode 3 Design of Steel Structures - Part 1-2: General Rules–Structural Fire Design. European Committee for Standardization (CEN), Brussels; 2005.
- [19] EN ISO 13919-1. Welding: electrons and laser beam welded joints – guidance on quality levels for imperfections – Part 1: steel. European Committee for Standardization (CEN), Brussels; 1997.
- [20] Huang, Y. and Young, B.. The art of coupon tests. *Journal of Constructional Steel Research* 2014;96:159–175.
- [21] EN ISO 6892-1. Metallic materials – tensile testing – Part 1: Method of test at room temperature. European Committee for Standardization (CEN), Brussels; 2009.
- [22] Mirambell, E. and Real, E.. On the calculation of deflections in structural stainless steel beams: an experimental and numerical investigation. *Journal of Constructional Steel Research* 2000;54(1):109–133.
- [23] Rasmussen, K.J.. Full-range stress–strain curves for stainless steel alloys. *Journal of Constructional Steel Research* 2003;59(1):47–61.
- [24] Gardner, L. and Yun, X.. Description of stress-strain curves for cold-formed steels. *Construction and Building Materials* 2018;189:527–538.
- [25] Arrayago, I., Real, E. and Gardner, L.. Description of stress-strain curves for stainless steel alloys. *Materials and Design* 2015;87:540–552.
- [26] Schafer, B.W. and Peköz, T.. Computational modeling of cold-formed steel: characterizing geometric imperfections and residual stresses. *Journal of Constructional Steel Research* 1998;47(3):193–210.
- [27] Gardner, L., Bu, Y. and Theofanous, M.. Laser-welded stainless steel I-sections: Residual stress measurements and column buckling tests. *Engineering Structures* 2016,127:536–548.
- [28] Wang, J., Afshan, S., Gkantou, M., Theofanous, M., Baniotopoulos, C. and Gardner, L.. Flexural behaviour of hot-finished high strength steel square and rectangular hollow sections. *Journal of Constructional Steel Research* 2016,121,97–109.
- [29] EN 1090-2, Execution of steel structures and aluminium structures. Part 2: Technical requirements for steel structures. European Committee for Standardization (CEN), Brussels; 2018.
- [30] Zhao, O., Rossi, B., Gardner, L. and Young, B.. Behaviour of structural stainless steel cross-sections under combined loading – Part I: Experimental study. *Engineering Structures* 2015;89:236–46.
- [31] Bu, Y. and Gardner, L.. Laser-welded stainless steel I-section beam-columns: Testing, simulation and design. *Engineering Structures* 2019;179:23–36.
- [32] Wang, Y., Burgess I., F. and Gillie, M.. Performance-based fire engineering of structures CRC press, 2012.
- [33] ISO 834, Fire resistance tests–Elements of building construction, International Organization for Standards, Geneva; 2014.
- [34] EN 1363-1, Fire resistance tests: Part 1–General requirements. European Committee for Standardization (CEN);2012.
- [35] Martins, A.D., Gonçalves, R. and Camotim, D.. Numerical simulation and design of stainless steel columns under fire conditions. *Engineering Structures* 2021;229:111628.
- [36] Zhao, O., Rossi, B., Gardner, L. and Young, B.. Behaviour of structural stainless steel cross-sections under combined loading – Part II: Numerical modelling and design approach. *Engineering Structures* 2015;89:247–

259.

- [37] Yang, L., Zhao, M., Gardner, L., Ning, K. and Wang, J.. Member stability of stainless steel welded I-section beam-columns. *Journal of Constructional Steel Research* 2019;155:33–45.
- [38] Design manual for structural stainless steel, Fourth Edition, Steel Construction Institute (SCI);2017.
- [39] Gardner, L., Insausti, A., Ng, K.T. and Ashraf, M.. Elevated temperature material properties of stainless steel alloys. *Journal of Constructional Steel Research* 2010;66(5):634–647.
- [40] Gardner, L., Bu, Y., Francis, P., Baddoo, N.R., Cashell, K.A. and McCann, F.. Elevated temperature material properties of stainless steel reinforcing bar. *Construction and Building Materials* 2016;114:977–997.
- [41] Chen, J. and Young, B.. Stress–strain curves for stainless steel at elevated temperatures. *Engineering Structures* 2006;28(2):229–239.
- [42] Xing, Z., Kucukler, M. and Gardner, L.. Local buckling of stainless steel plates in fire. *Thin-Walled Structures* 2020;148,106570.
- [43] Kucukler, M., Xing, Z. and Gardner, L.. Behaviour and design of stainless steel I-section columns in fire. *Journal of Constructional Steel Research* 2020;165,105890.
- [44] Bambach, M.R. and Rasmussen, K.J.. Effective widths of unstiffened elements with stress gradient. *Journal of Structural Engineering* 2004;130(10):1611–1619.
- [45] Gardner, L., Insausti, A., Ng, K. T., and Ashraf, M.. Elevated temperature material properties of stainless steel alloys. *Journal of Constructional Steel Research* 2010;66(5):634–647.
- [46] Knobloch, M., Pauli, J. and Fontana, M.. Influence of the strain-rate on the mechanical properties of mild carbon steel at elevated temperatures. *Materials & Design* 2013;49:553–565.
- [47] Afshan, S.. Structural behaviour of cold-formed stainless steel tubular members. Ph.D. thesis, Imperial College London UK, 2013.
- [48] Twilt, L.. Strength and deformation properties of steel at elevated temperatures: Some practical implications. *Fire Safety Journal* 1988;13(1),9–15.

8. Figures

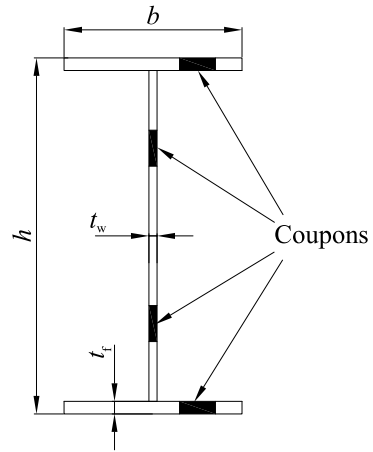


Figure 1: Cross-section labelling system and locations of tensile coupons

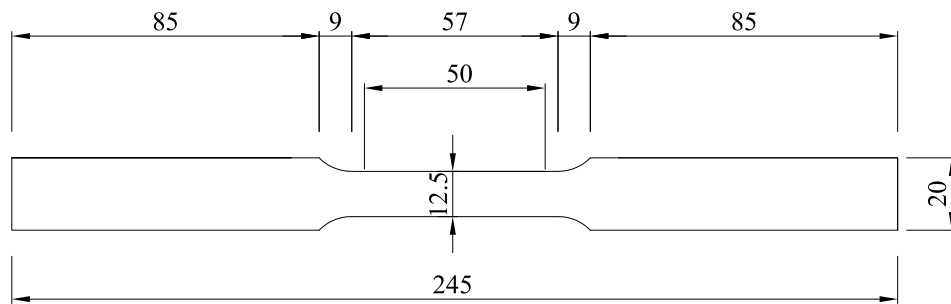


Figure 2: Dimensions of tensile coupon (dimensions in mm)

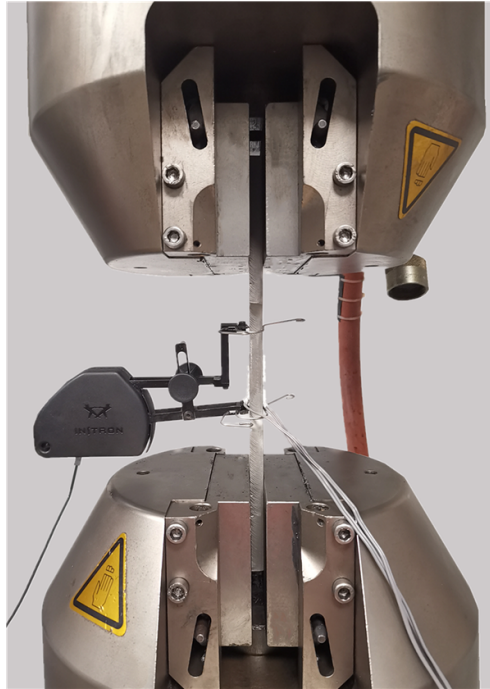
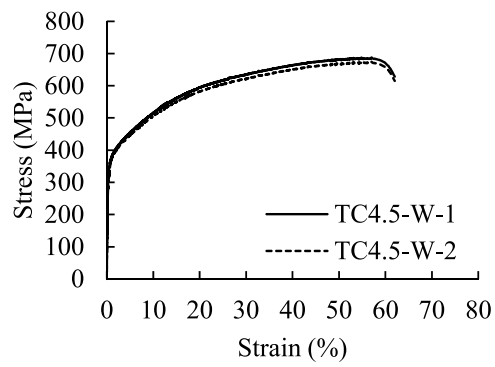
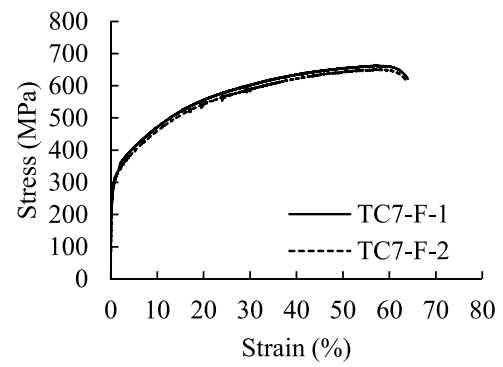


Figure 3: Tensile coupon test setup

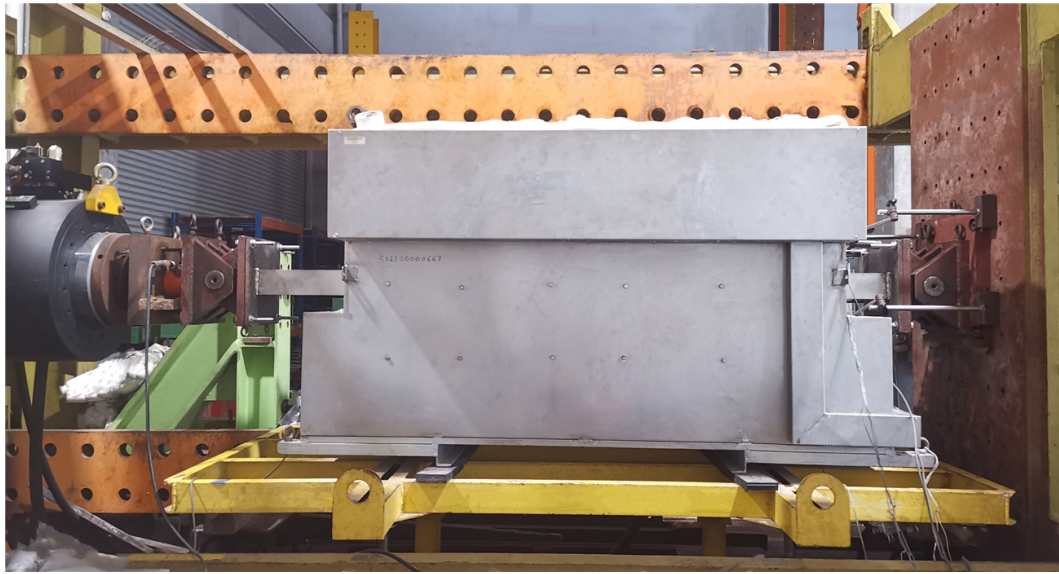


(a) Tensile coupon with 4.5 mm thickness (web)

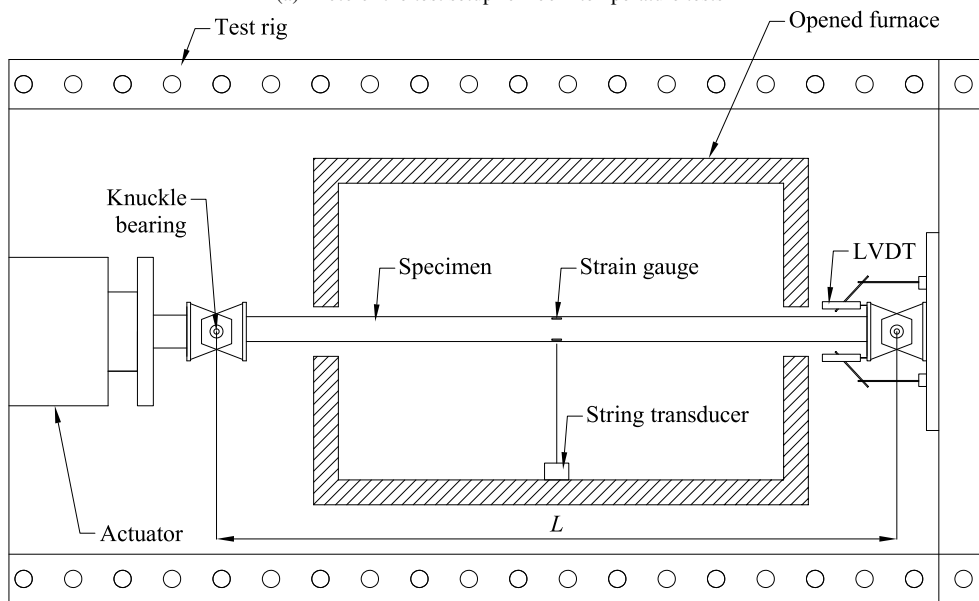


(b) Tensile coupon with 7 mm thickness (flange)

Figure 4: Measured room temperature stress-strain curves obtained from tensile coupon tests



(a) Photo of the test setup for room temperature tests



(b) Schematic drawing of the room temperature beam-column test setup

Figure 5: Beam-column test setup for room temperature tests



Figure 6: Imperfection measurement setup

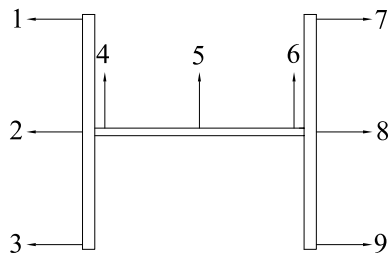
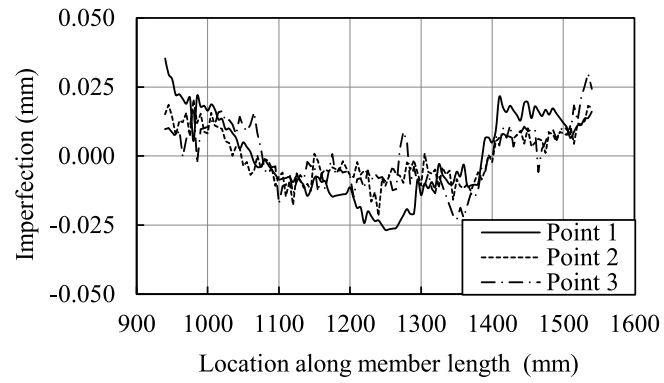
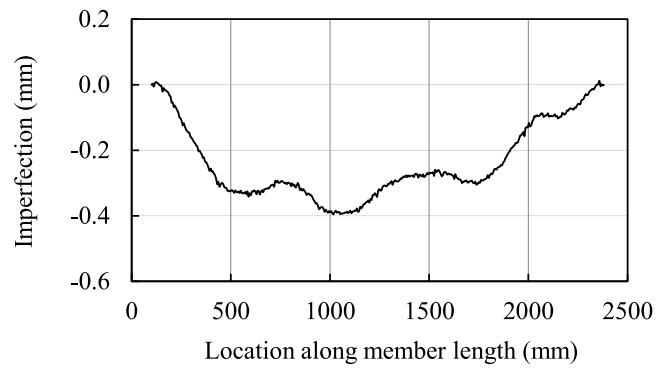


Figure 7: Imperfection measurement locations



(a) Local geometric imperfection distributions for top flange



(b) Initial global geometric imperfection distribution

Figure 8: Typical measured imperfection distributions; shown for specimen BC-Z10-20C

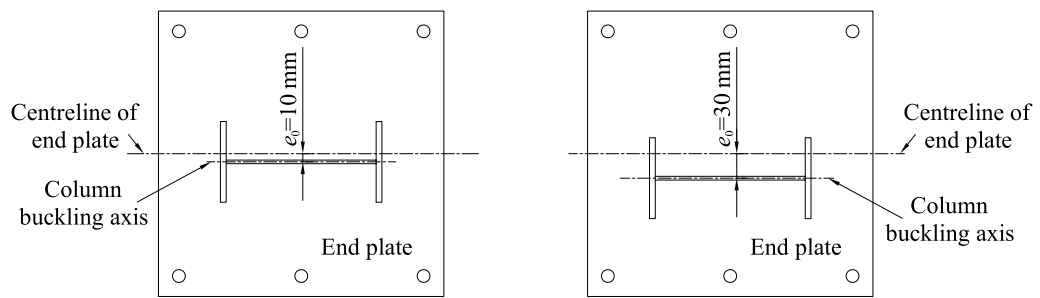


Figure 9: Positioning of specimens on end plates

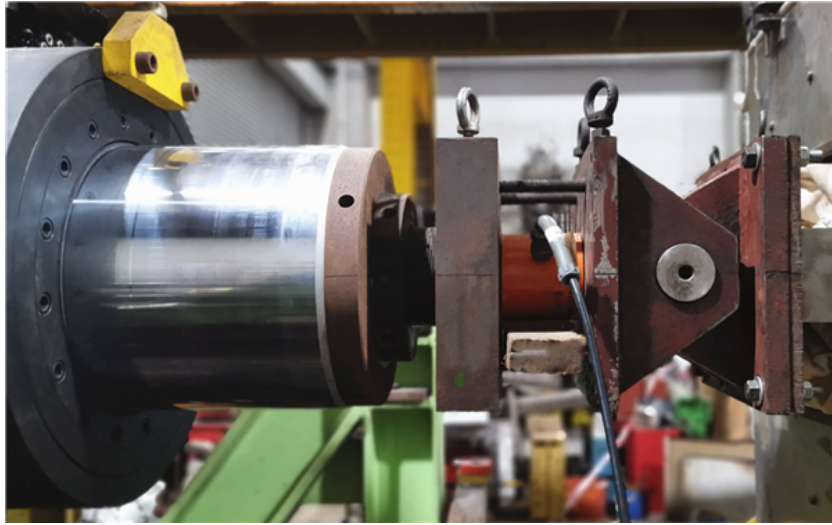


Figure 10: Details of loading system used in the experiments

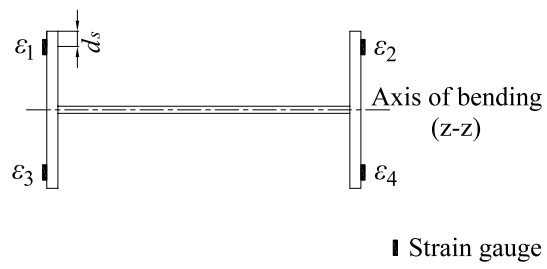


Figure 11: Strain gauge arrangement adopted at the mid-height of the specimens



Figure 12: Typical failure mode from room temperature tests, showing flexural buckling about the minor axis, illustrated for specimen BC-Z30-20C

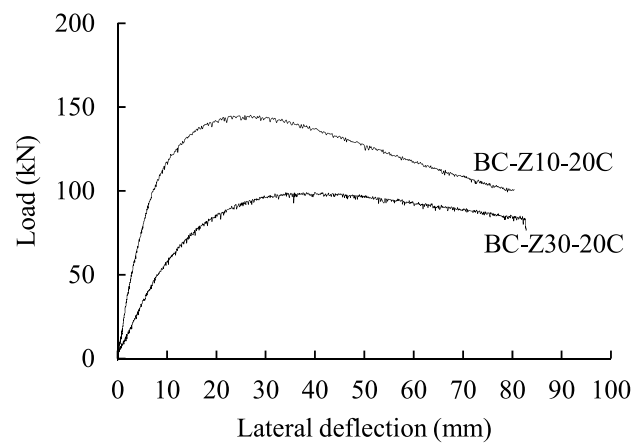
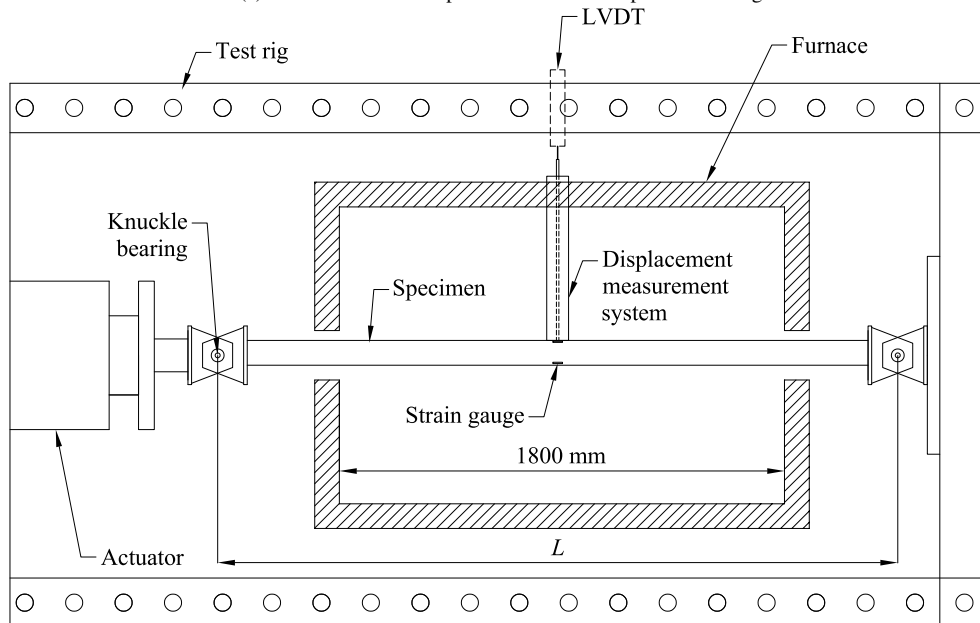


Figure 13: Load-lateral deflection curves for beam-column tests at room temperature



(a) Photo of the test setup for the elevated temperature testing



(b) Schematic drawing of the elevated temperature beam-column test setup

Figure 14: Beam-column test setup for elevated temperature testing

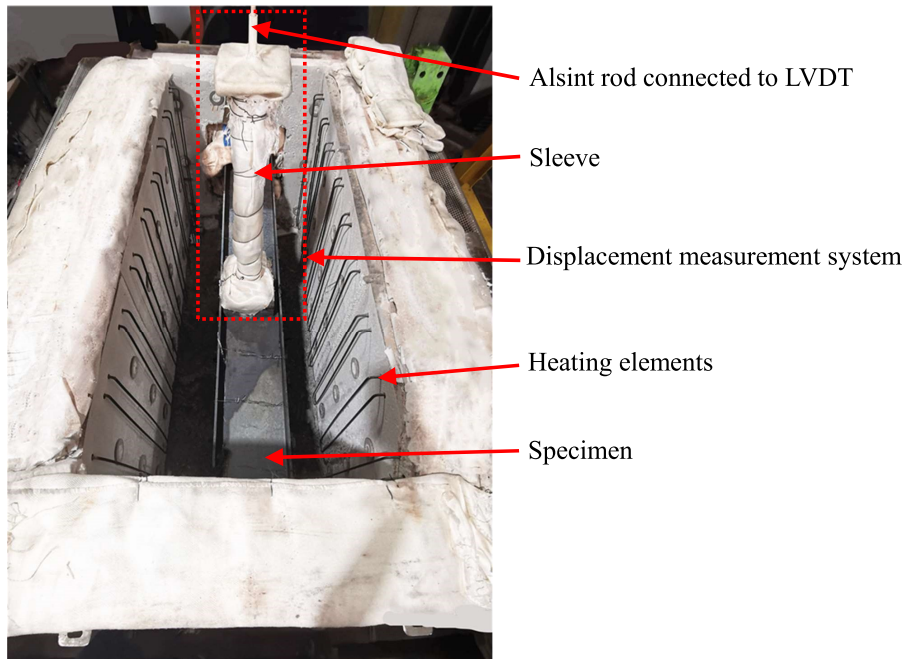


Figure 15: Inside of the furnace used in fire tests

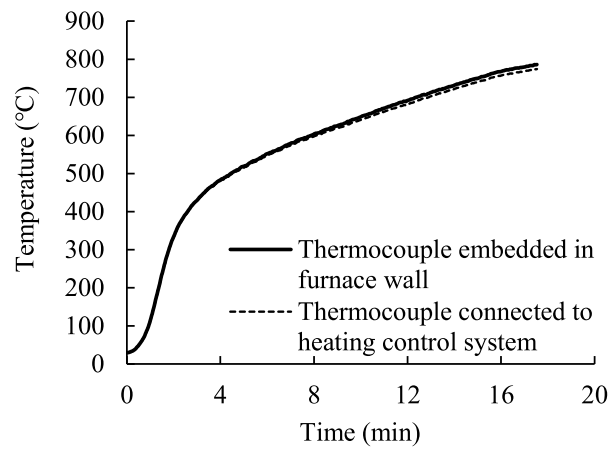


Figure 16: Furnace temperature measured by thermocouples

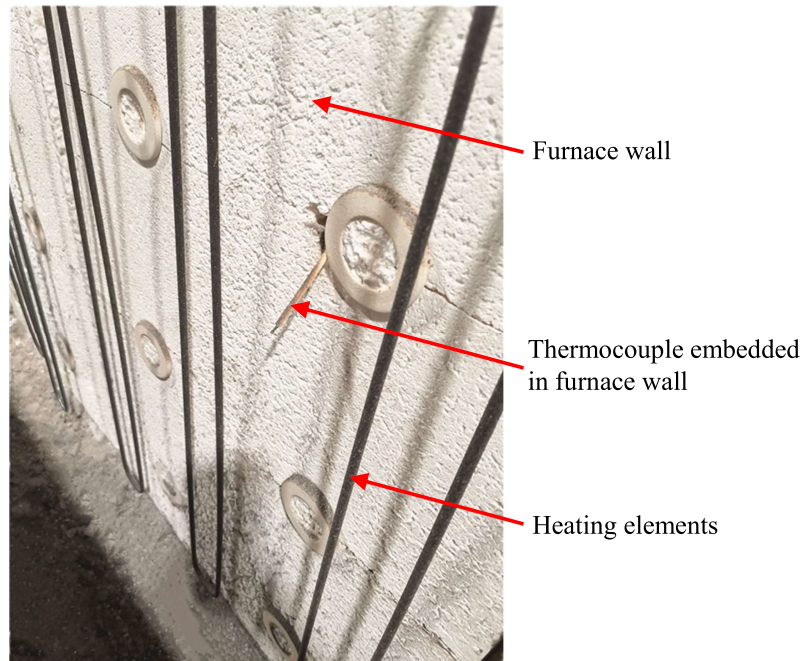


Figure 17: Thermocouple embedded in furnace wall

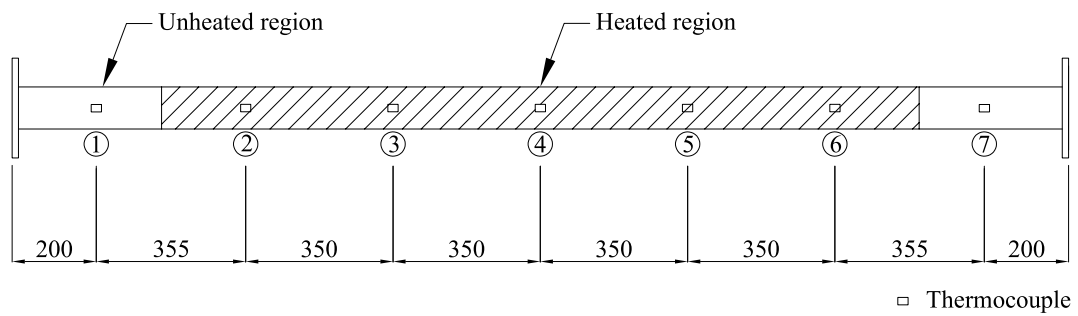


Figure 18: Locations of seven thermocouples mounted on specimens (dimensions in mm)

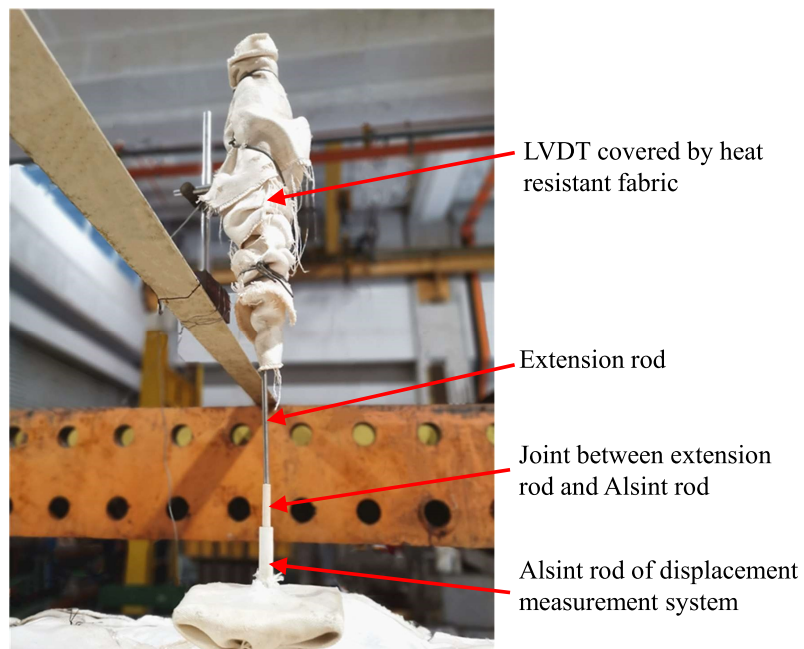


Figure 19: LVDT covered by heat resistant fabric used to measure mid-height lateral deflections of beam-column specimens



Figure 20: Failure modes of the beam-column fire test specimens with the 10 mm nominal eccentricity

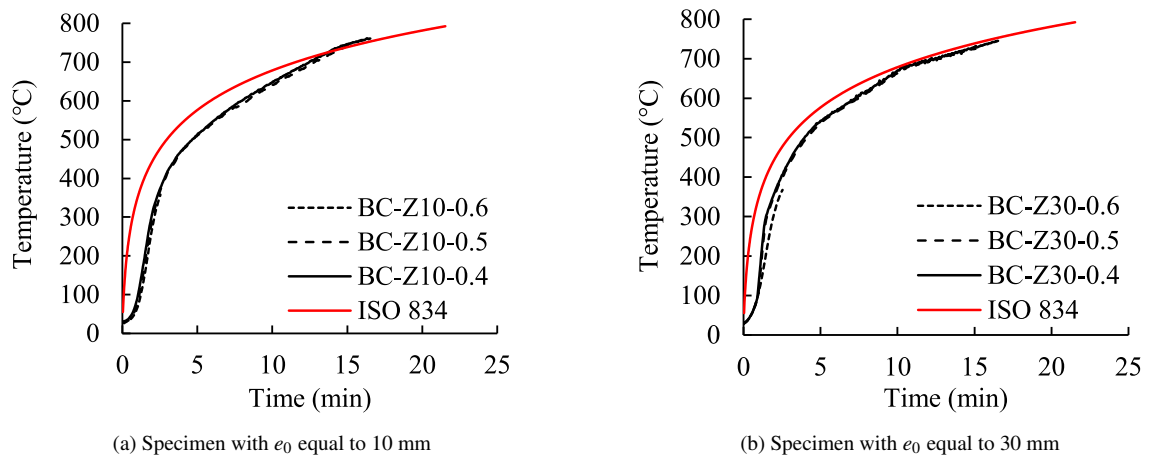
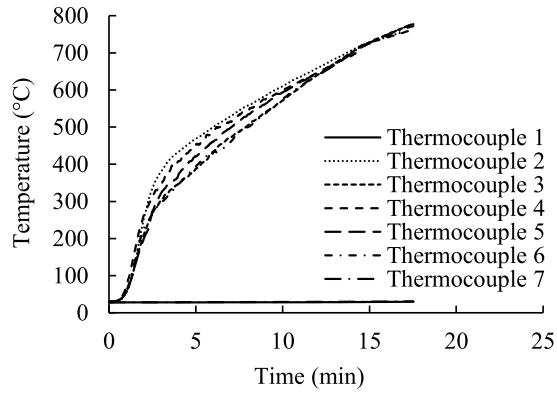
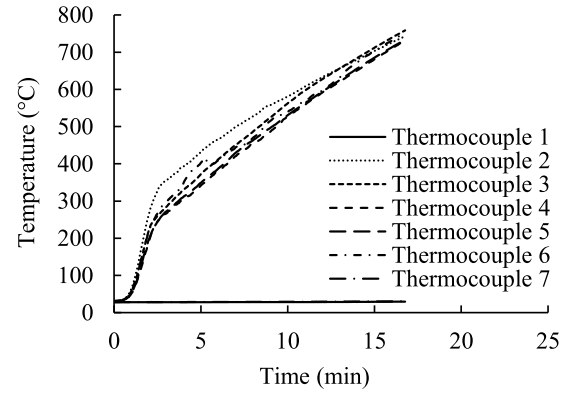


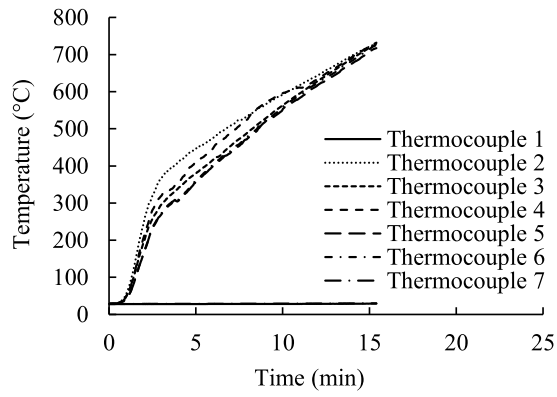
Figure 21: Comparison of the measured furnace temperature-time relationships with the ISO-834 standard fire curve



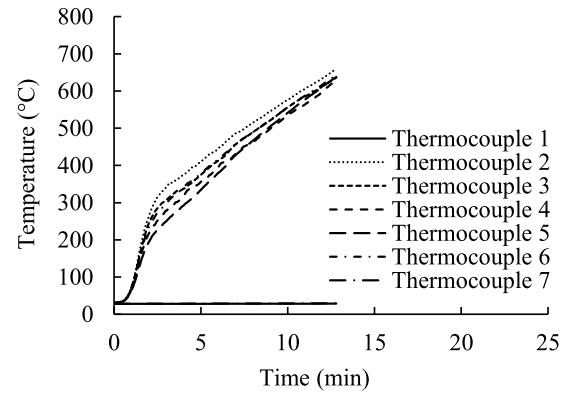
(a) BC-Z10-0.4



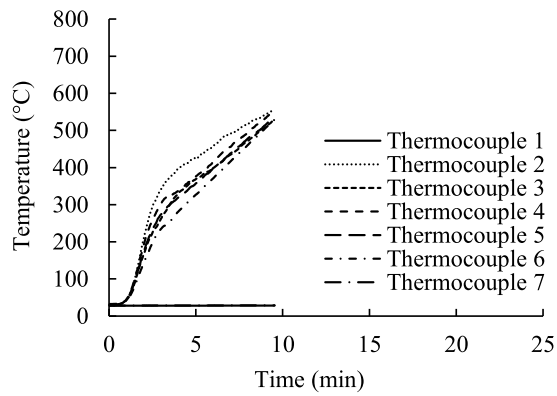
(b) BC-Z30-0.4



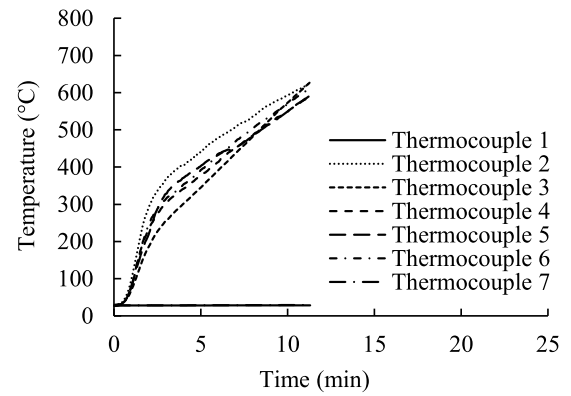
(c) BC-Z10-0.5



(d) BC-Z30-0.5

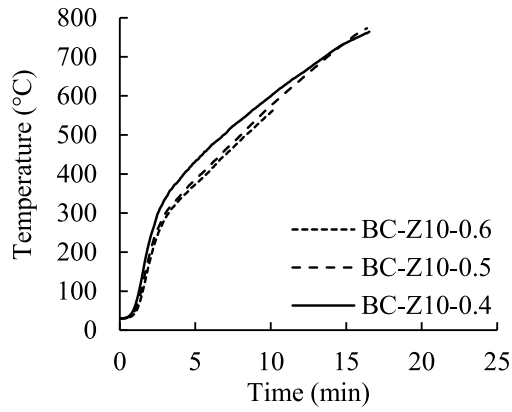


(e) BC-Z10-0.6

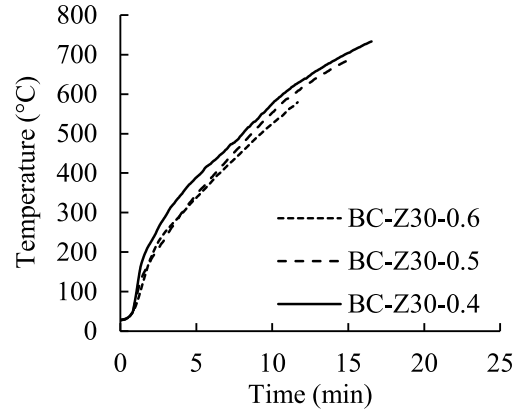


(f) BC-Z30-0.6

Figure 22: Specimen surface temperature versus time paths measured by thermocouples along specimen length

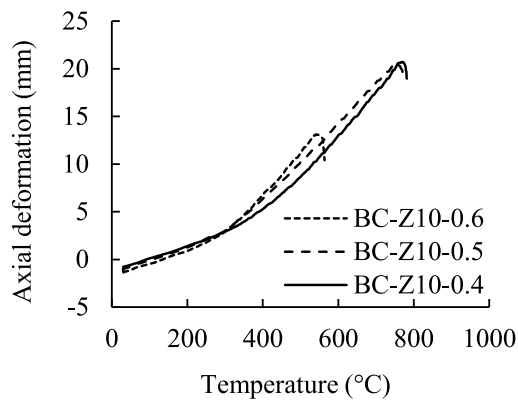


(a) Specimen with e_0 equal to 10 mm

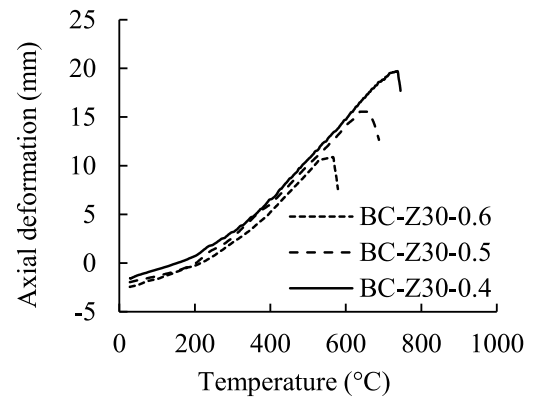


(b) Specimen with e_0 equal to 30 mm

Figure 23: Average measured specimen surface temperature-time paths for six fire test specimens



(a) Specimen with e_0 equal to 10 mm



(b) Specimen with e_0 equal to 30 mm

Figure 24: Axial deformation versus specimen temperature paths obtained from six fire tests, with positive deformations corresponding to expansion of the specimens

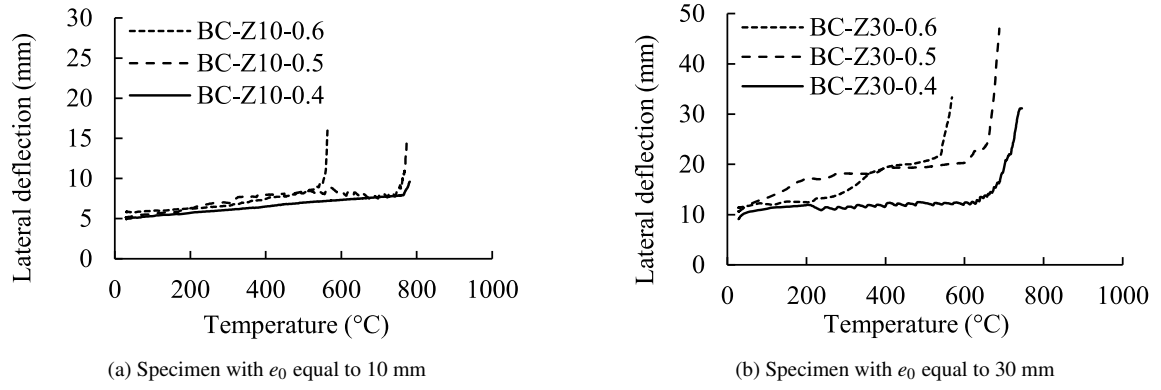


Figure 25: Lateral deflection versus specimen temperature paths obtained from six beam-column fire tests, with positive lateral deflections corresponding to downward deflections of the specimens

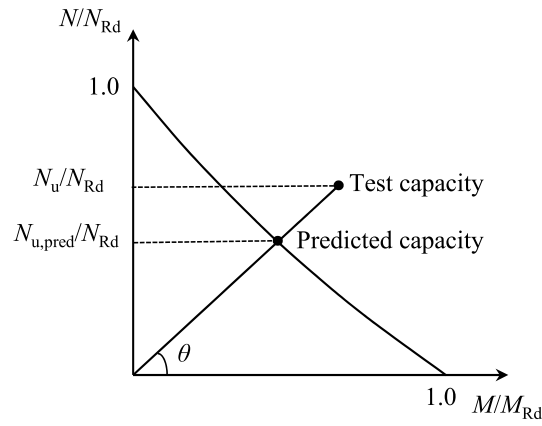


Figure 26: Definition of the radial angle θ on the axial load-moment interaction curve

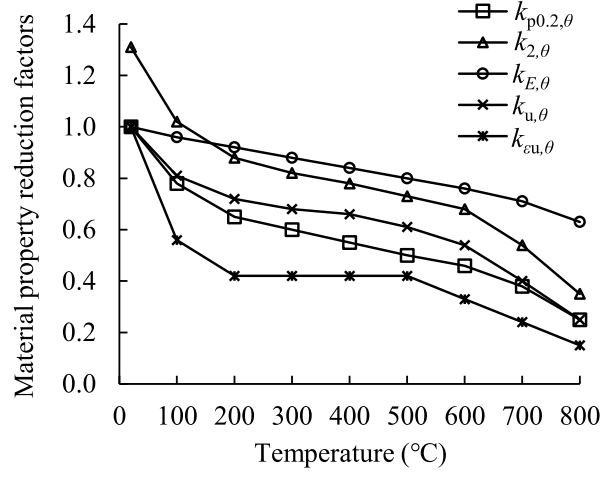


Figure 27: Strength ($k_{p0.2,\theta}$, $k_{2,\theta}$), stiffness ($k_{E,\theta}$) and ductility ($k_{\epsilon u,\theta}$) reduction factors for grade 1.4301 austenitic stainless steel at elevated temperatures from [38–41]

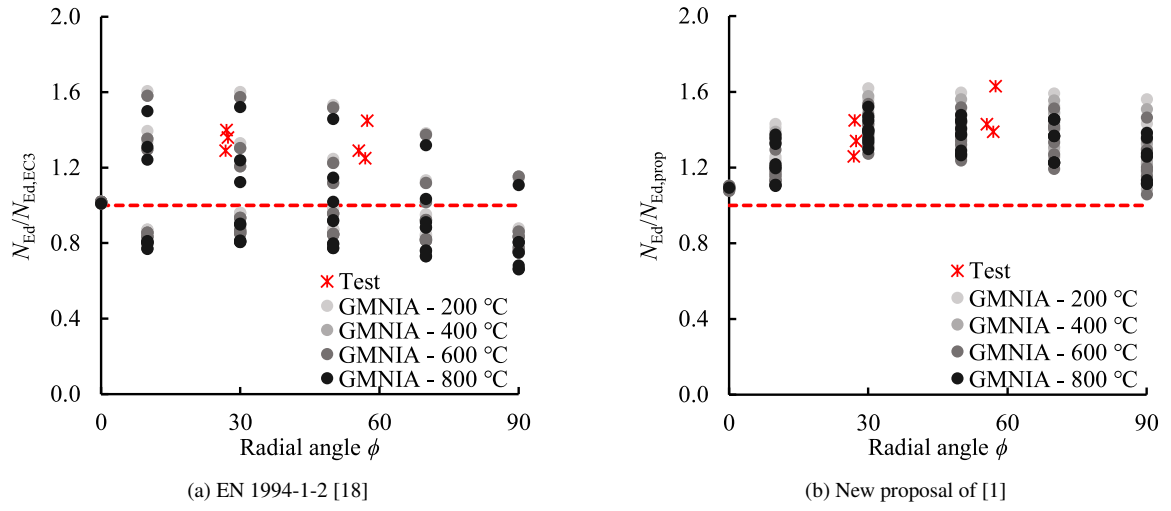


Figure 28: Comparison of accuracy of the new proposal of [1] against experimental and numerical results relative to EN 1993-1-2 [18]

9. Tables

Table 1: Chemical compositions provided in mill certificates

| Specimen | Material grade | C (%) | Si (%) | Mn (%) | P (%) | S (%) | Ni (%) | Cr (%) | N (%) |
|----------------|----------------|-------|--------|--------|-------|-------|--------|--------|-------|
| I-198×99×4.5×7 | 1.4301 | 0.026 | 0.41 | 1.37 | 0.032 | 0.001 | 8.00 | 18.01 | 0.070 |
| | | 0.024 | 0.40 | 1.38 | 0.031 | 0.002 | 8.05 | 18.05 | 0.069 |

Table 2: Material properties provided in mill certificates

| Specimen | $f_{y, \text{mill}}$ (N/mm ²) | $f_{p, 1.0, \text{mill}}$ (N/mm ²) | $f_{u, \text{mill}}$ (N/mm ²) | $\varepsilon_{f, \text{mill}}$ (%) |
|----------------|--|---|--|---------------------------------------|
| I-198×99×4.5×7 | 312 | 349 | 630 | 51 |
| | 313 | 348 | 625 | 52 |

Table 3: Key material properties obtained from tensile coupon tests

| ID | t (mm) | E (N/mm ²) | f_y (N/mm ²) | $f_{p1.0}$ (N/mm ²) | $f_{2.0}$ (N/mm ²) | f_u (N/mm ²) | ε_u (%) | ε_f (%) | R-O coefficient | |
|-----------|-------------|-----------------------------|-------------------------------|------------------------------------|-----------------------------------|-------------------------------|------------------------|------------------------|-----------------|-----|
| TC4.5-W-1 | 4.83 | 198200 | 324 | 386 | 405 | 688 | 57 | 70 | 4.7 | 2.8 |
| TC4.5-W-2 | 4.87 | 194600 | 298 | 376 | 399 | 681 | 55 | 69 | 5.5 | 3.2 |
| TC7-F-1 | 6.92 | 193700 | 263 | 320 | 356 | 665 | 57 | 74 | 5.7 | 2.8 |
| TC7-F-2 | 6.93 | 198800 | 254 | 323 | 343 | 649 | 54 | 77 | 6.7 | 2.6 |

Table 4: Geometric properties and imperfections of tested stainless steel I-section beam-column specimens

| ID | L (mm) | h (mm) | b (mm) | t_w (mm) | t_f (mm) | w_f (mm) | w_w (mm) | w_0 (mm) | v_0 (mm) |
|------------|-------------|-------------|-------------|---------------|---------------|---------------|---------------|---------------|---------------|
| BC-Z10-20C | 2751.50 | 198.08 | 99.41 | 4.95 | 6.93 | 0.03 | 0.06 | 0.06 | 0.38 |
| BC-Z10-0.6 | 2752.75 | 198.32 | 99.23 | 5.02 | 6.93 | 0.08 | 0.05 | 0.08 | 0.23 |
| BC-Z10-0.5 | 2752.25 | 198.26 | 99.53 | 4.96 | 6.93 | - | - | - | 0.17 |
| BC-Z10-0.4 | 2751.25 | 198.04 | 99.55 | 4.77 | 6.94 | - | - | - | 0.32 |
| BC-Z30-20C | 2751.25 | 198.31 | 99.48 | 4.84 | 6.96 | 0.05 | 0.05 | 0.05 | 0.27 |
| BC-Z30-0.6 | 2751.50 | 198.28 | 99.43 | 4.88 | 6.91 | 0.04 | 0.06 | 0.06 | 0.39 |
| BC-Z30-0.5 | 2753.25 | 198.24 | 99.64 | 4.87 | 6.92 | - | - | - | 0.43 |
| BC-Z30-0.4 | 2752.25 | 197.96 | 99.45 | 4.82 | 6.86 | - | - | - | 0.21 |

Table 5: Key experimental results of beam-column tests performed at room temperature

| ID | Total eccentricity $v_0 + e_0$ (mm) | Ultimate load N_u (kN) | Lateral displacement at N_u (mm) | Ultimate first order bending moment M_u (kNm) |
|------------|---|--------------------------------|--|---|
| BC-Z10-20C | 10.98 | 145 | 26.9 | 1.59 |
| BC-Z30-20C | 30.36 | 99 | 38.3 | 3.01 |

Table 6: Measured eccentricities, pre-applied loads and load ratios of specimens under compression and bending about the minor axis subjected to fire testing

| ID | Total eccentricity $v_0 + e_0$ (mm) | Pre-applied load (kN) | Load ratio n_r - |
|------------|--|--------------------------|-----------------------|
| BC-Z10-0.6 | 10.53 | 89 | 0.61 |
| BC-Z10-0.5 | 9.89 | 76 | 0.52 |
| BC-Z10-0.4 | 10.21 | 60 | 0.42 |
| BC-Z30-0.6 | 30.35 | 60 | 0.60 |
| BC-Z30-0.5 | 30.72 | 51 | 0.51 |
| BC-Z30-0.4 | 30.07 | 44 | 0.44 |

Table 7: Measured fire resistances from beam-column tests

| ID | Fire resistance $t_{fi,test}$ (min) | θ_{cr} (°C) |
|------------|--|-----------------------|
| BC-Z10-0.6 | 9.53 | 540 |
| BC-Z10-0.5 | 15.40 | 749 |
| BC-Z10-0.4 | 16.97 | 771 |
| BC-Z30-0.6 | 11.30 | 567 |
| BC-Z30-0.5 | 12.77 | 637 |
| BC-Z30-0.4 | 16.77 | 737 |

Table 8: Beam-column resistances in fire predicted by EN 1993-1-2 [18]

| ID | θ_{cr} (°C) | Pre-applied load $N_{Ed,test}$ (kN) | Predicted buckling resistance $N_{b,Rd,EC3}$ at θ_{cr} (kN) | $N_{Ed,test}/N_{b,Rd,EC3}$ |
|------------|-----------------------|---|--|----------------------------|
| BC-Z10-0.6 | 540 | 89 | 69 | 1.29 |
| BC-Z10-0.5 | 749 | 76 | 52 | 1.45 |
| BC-Z10-0.4 | 771 | 60 | 48 | 1.25 |
| BC-Z30-0.6 | 567 | 60 | 42 | 1.40 |
| BC-Z30-0.5 | 637 | 51 | 39 | 1.29 |
| BC-Z30-0.4 | 737 | 44 | 32 | 1.36 |

Table 9: Beam-column resistances in fire predicted by new proposed method [1]

| ID | θ_{cr} | Pre-applied load | Predicted buckling resistance | $N_{Ed,test}/N_{b,Rd,Prop}$ |
|-----------|---------------|-----------------------|--|-----------------------------|
| | (°C) | $N_{Ed,test}$ (kN) | $N_{b,Rd,Prop}$ at θ_{cr} (kN) | |
| BC1-Z10-1 | 540 | 89 | 62 | 1.43 |
| BC1-Z10-2 | 749 | 76 | 47 | 1.63 |
| BC1-Z10-3 | 771 | 60 | 43 | 1.39 |
| BC1-Z30-1 | 567 | 60 | 41 | 1.45 |
| BC1-Z30-2 | 637 | 51 | 40 | 1.26 |
| BC1-Z30-3 | 737 | 44 | 33 | 1.34 |